NANO · MICRO
small

Supporting Information

for *Small*, DOI 10.1002/smll.202505647

Spectrally-Tailored Hygroscopic Hydrogels with Janus Interfaces for Hybrid Passive Cooling of Solar Cells

Shuai Li, Suxu Wang, Jun Zhao, Zhihang Wang, Petri Murto, Liangmin Yu, Junwu Chen* and Xiaofeng Xu**

Supporting Information

Spectrally-Tailored Hygroscopic Hydrogels with Janus Interfaces for Hybrid Passive Cooling of Solar Cells

Shuai Li, *Suxu Wang*, *Jun Zhao*, *Zhihang Wang**, *Petri Murto*, *Liangmin Yu*, *Junwu Chen** & *Xiaofeng Xu**

S. Li, S. Wang, J. Zhao

Prof. X. Xu, email: xuxiaofeng@ouc.edu.cn

College of Materials Science and Engineering, Ocean University of China, Qingdao 266100, China.

Dr. Z. Wang, email: z.wang@derby.ac.uk

School of Engineering, College of Science and Engineering, University of Derby, Markeaton Street, Derby DE22 3AW, United Kingdom.

Department of Materials Science and Metallurgy, University of Cambridge, 27 Charles Babbage Road, Cambridge, CB3 0FS, United Kingdom.

Dr. P. Murto

Department of Chemistry and Materials Science, Aalto University, Kemistintie 1, 02150 Espoo, Finland.

Prof. L. Yu

Key Laboratory of Marine Chemistry Theory and Technology, Ministry of Education, Ocean University of China, Qingdao 266100, China.

Prof. J. Chen, email: psjwchen@scut.edu.cn

Institute of Polymer Optoelectronic Materials & Devices, State Key Laboratory of Luminescent Materials & Devices, South China University of Technology, Guangzhou 510640, China

Table of Contents

1. Materials

2-(*N*-3-Sulfopropyl-*N*,*N*-dimethyl ammonium)ethyl methacrylate (DMAPS), *N*-hydroxyethyl acrylamide (HEAA), polyanionic cellulose (PAC), *α*-ketoglutaric acid (*α*-T), poly(ethylene glycol) diacrylate (PEGDA), *N*,*N*'-methylenebisacrylamide (MBA) and lithium chloride (LiCl) were purchased from Sinopharm Chemical Reagent Co., Ltd. Electron-donor PBDB-TF-T10 was synthesized according to our previous report.[1] Non-fullerene electron-acceptor BTP-eC9 and fullerene electron-acceptor $PC_{71}BM$ were purchased from Solarmer Energy, Inc.

2. Material characterization

^1H NMR spectra were recorded using an Agilent 600 MHz NMR spectrometer (Agilent Technologies). X-ray diffraction (XRD) analysis was carried out on a Rigaku Miniflex 600 diffractometer. Storage modulus (G′) and loss modulus (G″) were measured by rotational rheometer (MCR302, Anton Paar). The tensile, compression tests were performed using a universal mechanical testing system equipped digital force gauges (M5-100, Mark-10, accuracy: 0.02 N) and a force test stand (ESM 303, Mark-10). The UV−Vis−NIR absorption spectra were recorded with LAMBDA 1050+ spectrometer equipped with an integrating sphere. Water vapor sorption of all samples was evaluated in an artificial climate chamber (RGC-160D, Youke). The morphologies and elemental mapping were characterized by a scanning electron microscope (VEGA3, TESCAN) in combination with energy dispersive X-ray spectrometry. $J-V$ curves of solar cells were recorded in backward scan direction by using a Keithley 2400 source meter under a solar simulator (Oriel Sol3A, 69920, Newport). The light intensity was calibrated by using a Si-based power meter (PT-SI-SRC, Pharos). For the EQE measurements, the photocurrent was measured by using a Keithley 485 picoammeter under monochromatic light (MS257) illumination across the PSCs. The current was recorded as the voltage over a 50 Ω resistance and converted to a EQE profile by comparing the data with a calibrated Si reference cell.

3. Chemical structure characterization

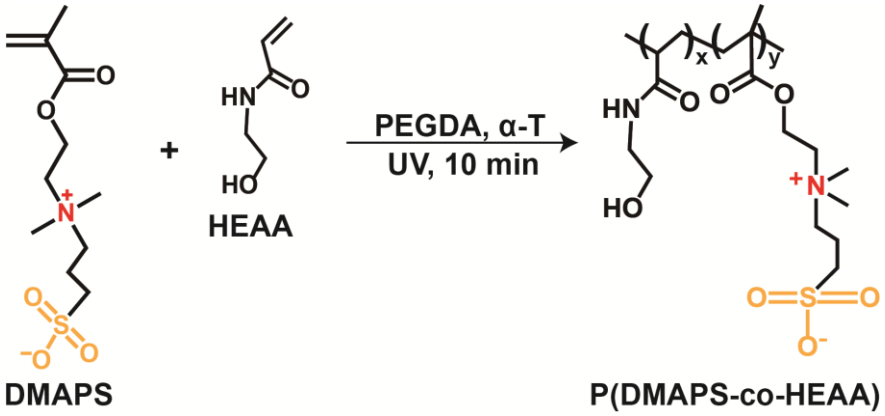

Figure S1. Synthetic route of P(DMAPS-*co*-HEAA).

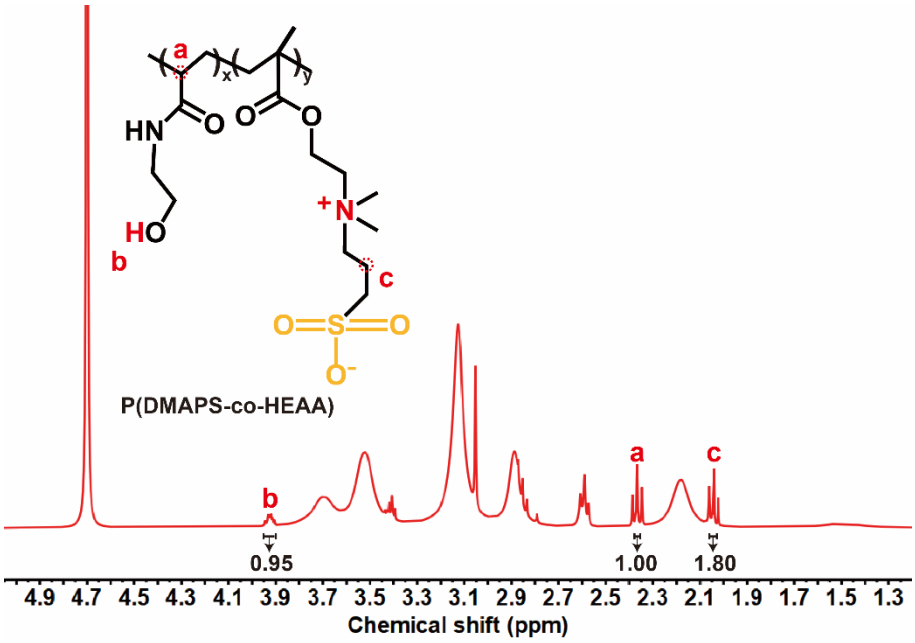

Figure S2. ^{1}H NMR spectrum of P(DMAPS-*co*-HEAA).

4. Cyclic compression test of M2

Table S1. Summary of material components in a series of M2s.

	Polymer (wt%)[a]	DMAPS (wt%)[a]	HEAA (wt%)[a]	DMAPS:HEAA[b]	LiCl (wt%)[a]	Water (wt%)
H1	50	35.4	14.6	1:1	10	40
H2	60	42.6	17.4	1:1	10	30
H3	65	46.0	19.0	1:1	5	25
H4	65	46.0	19.0	1:1	8	25
H5	65	65.0	0	1:0	10	25
H6	65	53.8	11.2	2:1	10	25
H7	65	46.0	19.0	1:1	10	25
H8	65	35.6	29.4	1:2	10	25
H9	65	0	65.0	0:1	10	25

[a] mass ratio relative to total hydrogel and [b] initial molar ratio of two monomers

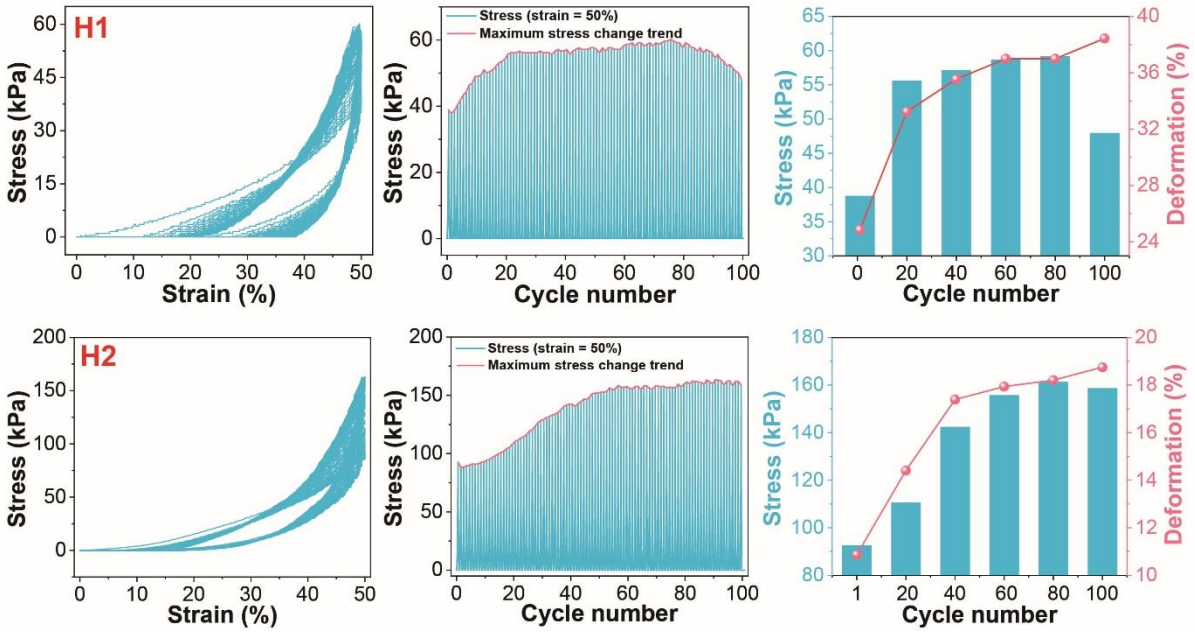

Figure S3. Cyclic compression testing of M2 (H1 and H2) with different P(DMAPS-*co*-HEAA) contents.

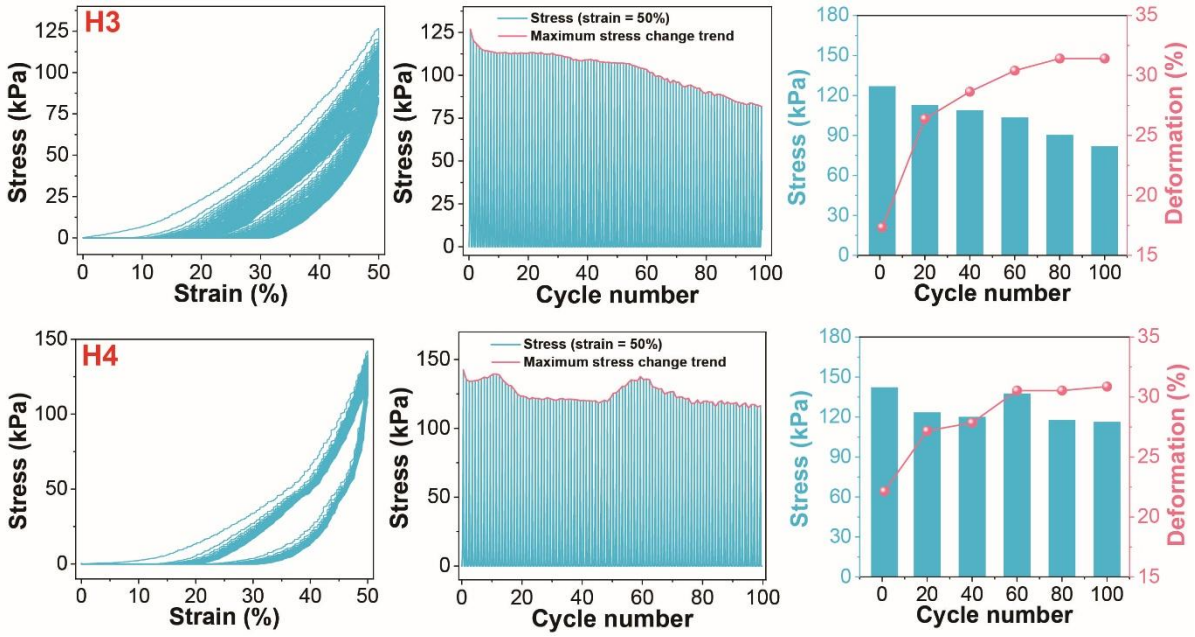

Figure S4. Cyclic compression testing of M2 (H3 and H4) with different LiCl contents.

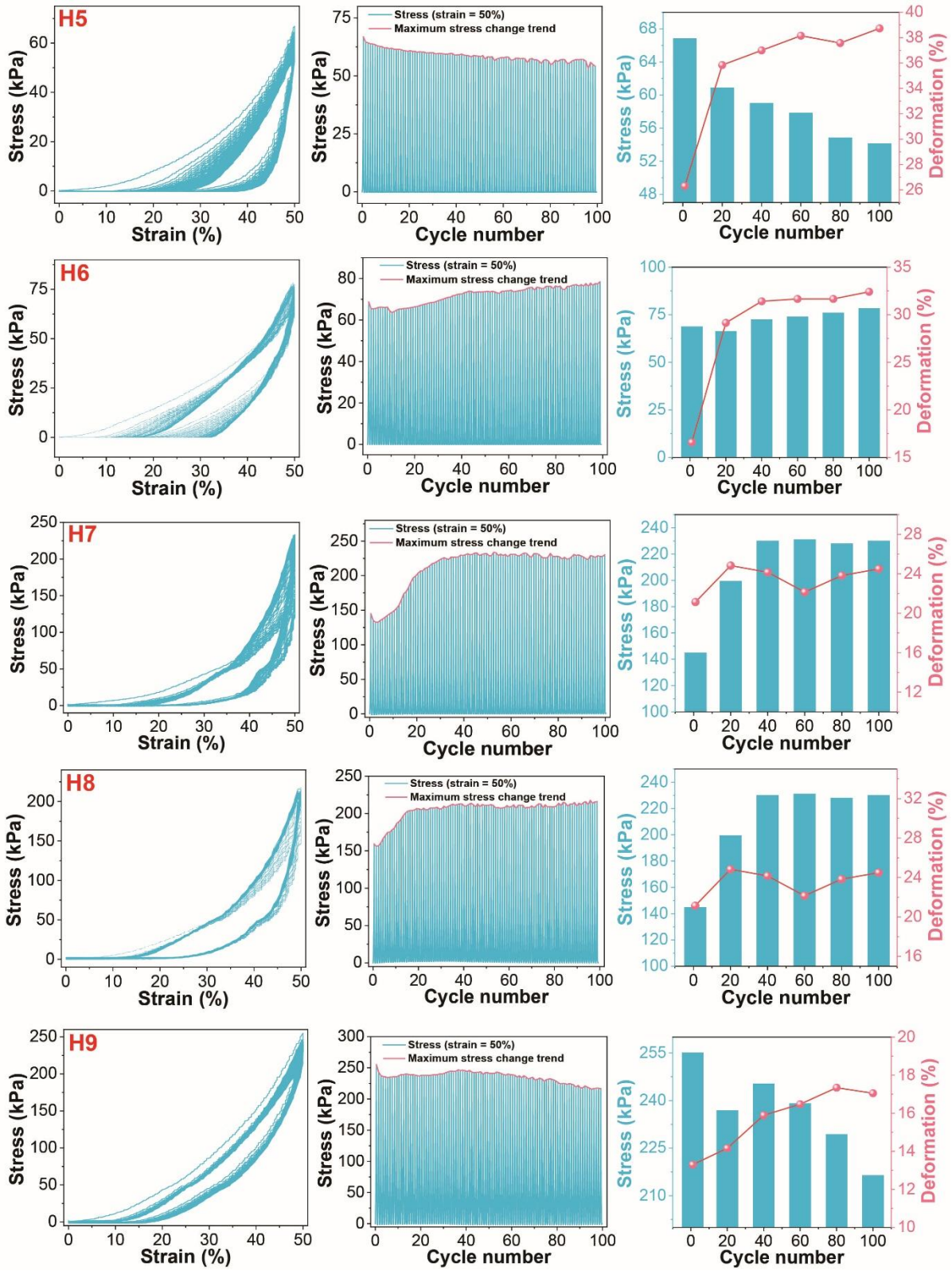

Figure S5. Cyclic compression testing of M2 (H5 − H9) with varying DMAPS and HEAA molar ratios.

5. Tensile testing of hydrogels

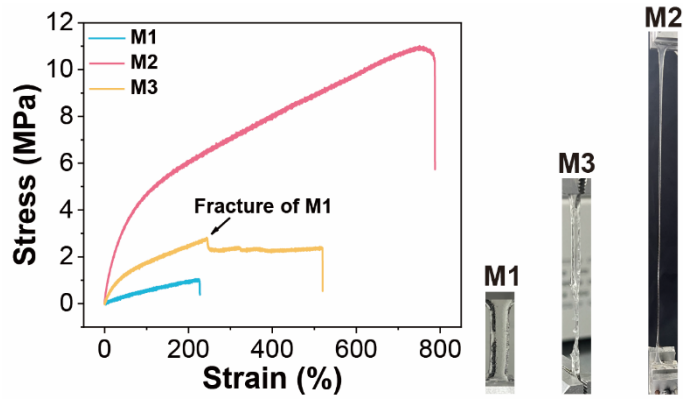

Figure S6. Tensile stress−strain curves of M1, M2 and M3.

6. Water vapor sorption of M2

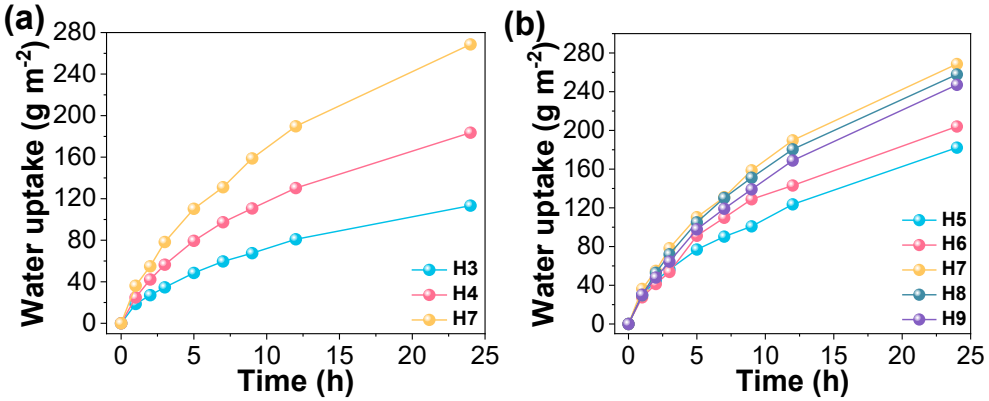

Figure S7. Water vapor sorption of M2 with (a) different LiCl contents and (b) varying DMAPS and HEAA molar ratios under 90% RH and at 25 °C.

7. Chemical structure of PAC

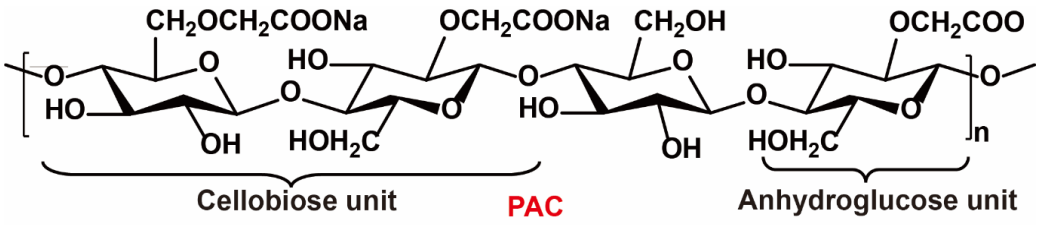

Figure S8. Chemical structure of PAC.

8. Water vapor sorption of M1

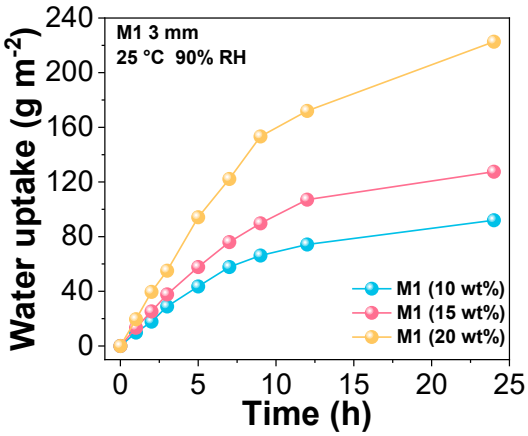

Figure S9. Water vapor sorption of M1 with different LiCl contents under 90% RH and at 25 °C.

9. Schematic illustration of interfacial interactions

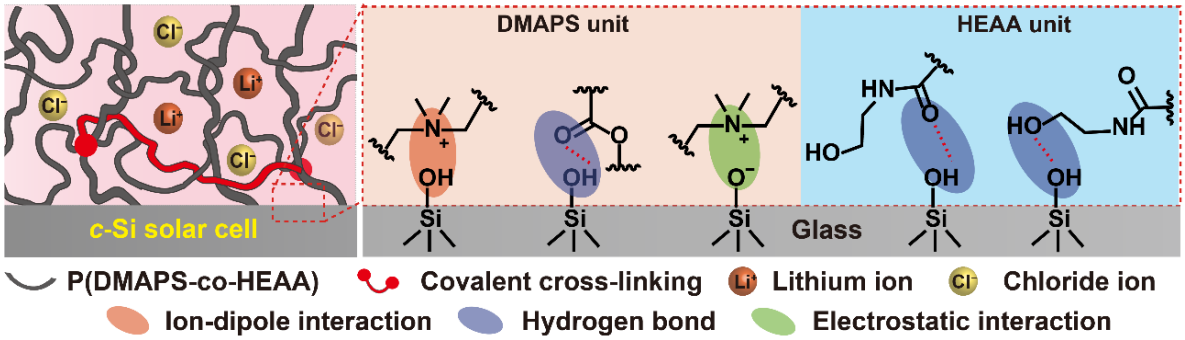

Figure S10. Schematic illustration of interfacial interactions within a M2/glass interface.

10. Adhesion characterization on PET and EVA

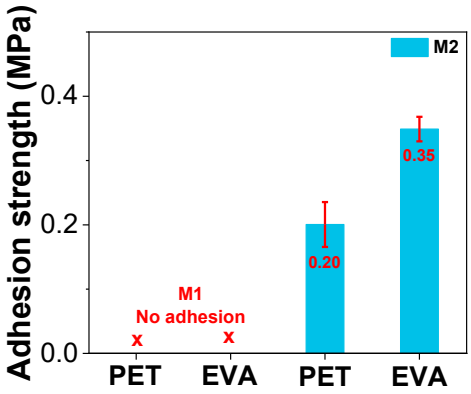

Figure S11. Adhesion strengths of M1 and M2 on the PET and EVA substrates.

11. Transmittance spectra of M1 and M2

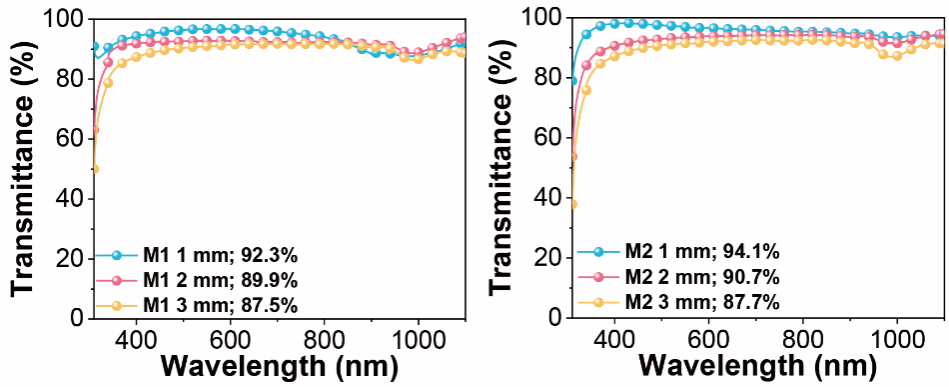

Figure S12. Transmittance spectra of M1 and M2 with different thickness (1 − 3 mm).

Transmission spectra of hydrogels across the range of 300 to 1100 nm were measured using an UV−Vis−NIR spectrophotometer. Effective transmittance ($T_{VIS-NIR}$) of hydrogels can be expressed using equation S1,

$$T_{VIS-NIR} = \frac{\int_{300}^{1100} \varphi(\lambda) T(\lambda) d(\lambda)}{\int_{300}^{1100} \varphi(\lambda) d(\lambda)} \quad \text{(S1)}$$

where the T(λ) denotes the recorded transmittance at a particular wavelength, and φ(λ) is the solar irradiance spectrum for AM 1.5.

12. Water vapor sorption of M3 with different thickness

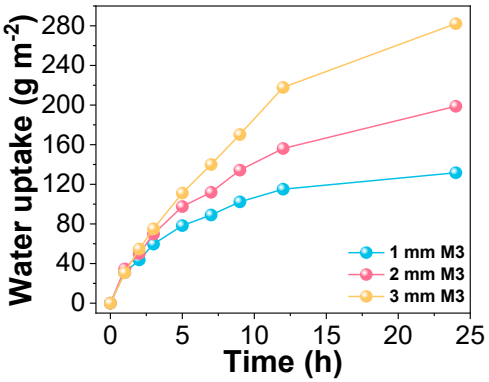

Figure S13. Water vapor sorption of M3 with different thickness (1 − 3 mm) under 90% RH and at 25 °C.

13. Calculation of vapor pressure of LiCl solutions and humid air

The vapor pressure of LiCl solution, denoted as $P_{sol}(\xi, T)$, can be expressed through its functional dependence on both $P_{H_2O}(T)$ (the saturation pressure of pure water) and the mass fraction of LiCl (ξ). This relationship has been quantitatively established in previous studies[2-3], where the solution's vapor pressure is correlated with these parameters through the following equations,

$$\frac{P_{sol}(\xi,T)}{P_{H_2O}(T)} = \pi_{25} f(\xi,\theta) \qquad \text{(S2)}$$

$$f(\xi,\theta) = A + B\theta \qquad \text{(S3)}$$

$$A = 2 - \left[1 + \left(\frac{\xi}{\pi_0}\right)^{\pi_1}\right]^{\pi_2} \qquad \text{(S4)}$$

$$B = \left[1 + \left(\frac{\xi}{\pi_3}\right)^{\pi_4}\right]^{\pi_5} - 1 \qquad \text{(S5)}$$

$$\theta = \frac{T}{T_{c,H_2O}} \qquad \text{(S6)}$$

$$\pi_{25} = 1 - \left[1 + \left(\frac{\xi}{\pi_6} \right)^{\pi_7} \right]^{\pi_8} - \pi_9 e^{-\frac{(\xi - 0.1)^2}{0.0005}} \qquad \text{(S7)}$$

where the parameters of $\pi_0 - \pi_9$ are given in **Table S2**.

Table S2. Parameters for the vapor pressure equation.

π_0	π_1	π_2	π_3	π_4	π_5	π_6	π_7	π_8	π_9
0.28	4.30	0.60	0.21	5.10	0.49	0.362	−4.75	−0.4	0.03

Based on Equation S1−S6, the vapor pressure curves of 10, 20 and 30 wt% LiCl solutions at various temperatures are plotted in **Figure 3a**.

Water vapor saturation pressure ($P_{\text{sat.}}$) is temperature-dependent and can be described using the empirical August-Roche-Magnus (AERK) formulation, expressed by equation S8,l[4]

$$P_{\text{sat.}}(T) = 610.94 \exp\left(\frac{17.625T}{243.04 + T} \right) \qquad \text{(S8)}$$

The vapor pressure (P_{vapor}) in air with varying humidity levels can be calculated using the definition of relative humidity (Φ), as expressed in Equation S9,[4]

$$\Phi = \frac{P_{vapor}}{P_{\text{sat.}}(T)} \qquad \text{(S9)}$$

The P_{vapor} curves for different temperatures at 30%, 60%, and 90% RH, and $P_{\text{sat.}}$ in humid air were derived from equations S8−S9 and are plotted in **Figure 3a**.

14. Water contact angle measurements

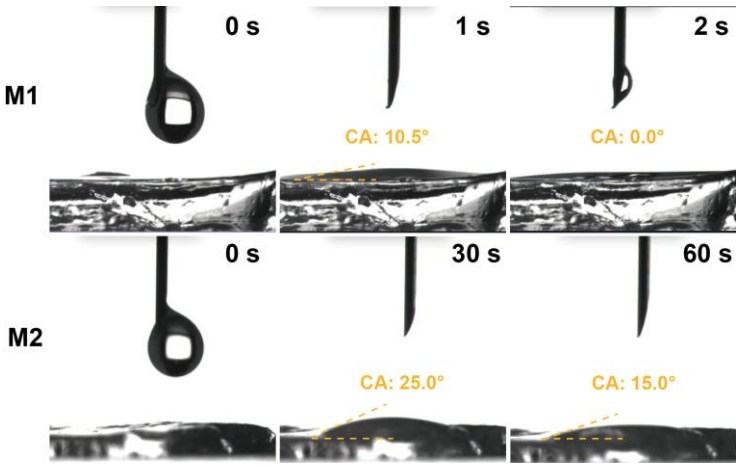

Figure S14. Water contact angle measurements on the surfaces of M1 and M2.

15. Water diffusion mechanisms

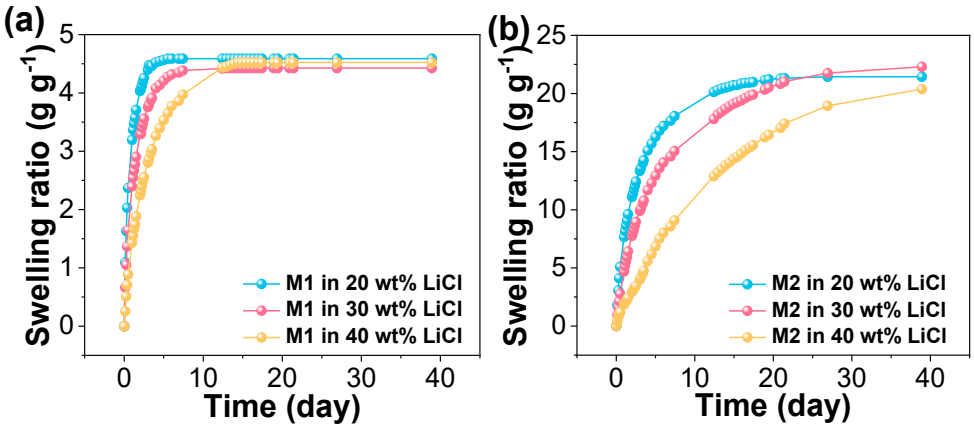

Figure S15. Water uptake of (a) M1 and (b) M2 in LiCl solutions of varying concentrations for a specific time period.

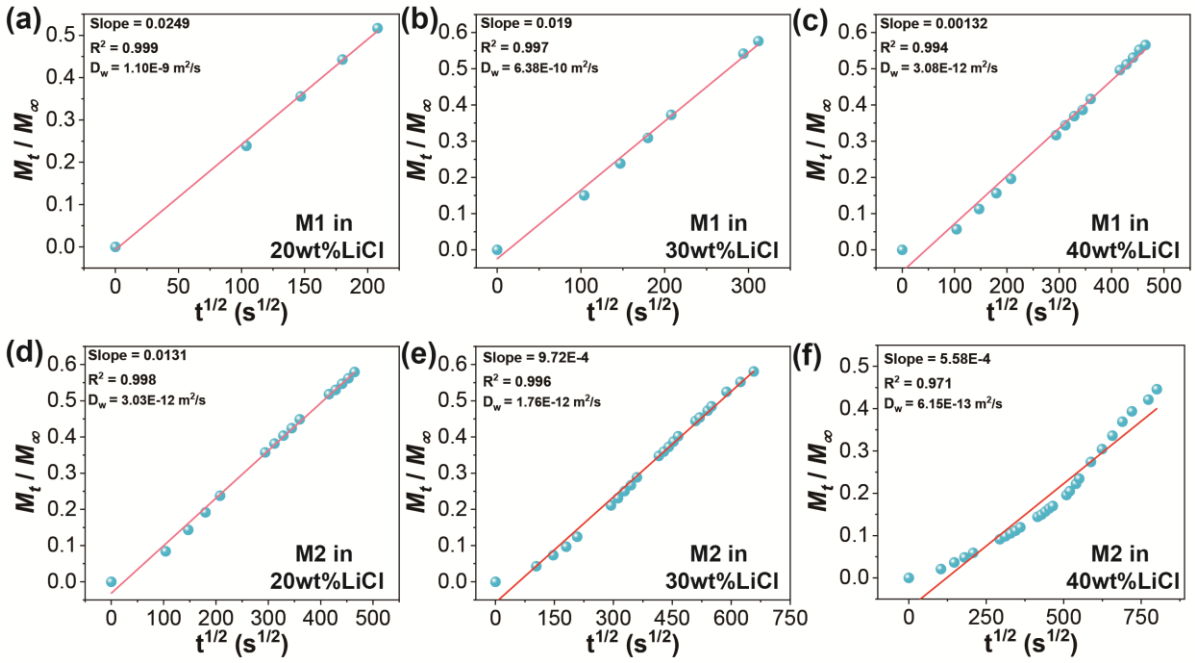

Figure S16. Linear fitting of M_t/M_∞ as a function of $t^{1/2}$ based on the date from M1 and M2 swelling in different LiCl solutions.

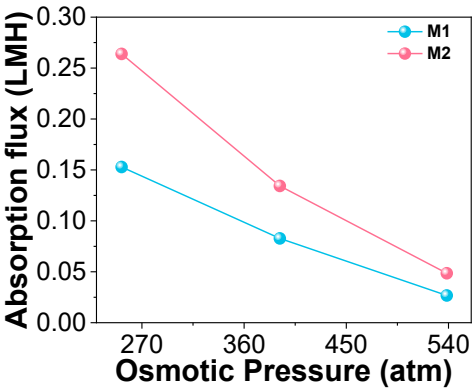

Figure S17. Water absorption fluxes of M1 and M2 in different LiCl solutions.

16. Surface temperature characterization

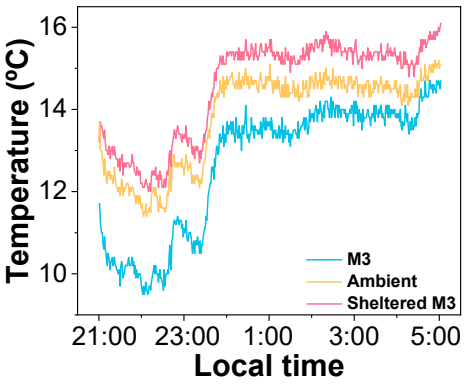

Figure S18. Temperature variations of the ambient environment, PMMA-sheltered M3 and M3-covered solar cell over night.

The effective humidity (Φ') near the M3 interface and the ambient RH (Φ) can be expressed as equations S10−S11,

$$\Phi' = \frac{P_{vapor}}{P_{\text{sat.}}\left(T_{\text{M3}}\right)} \qquad \text{(S10)}$$

$$\Phi = \frac{P_{vapor}}{P_{\text{sat.}}\left(T_{\text{Amb}}\right)} \qquad \text{(S11)}$$

where T_{M3} and T_{Amb} denote the surface temperature of the M3 and ambient temperature, respectively, and P_{vapor} represents the ambient vapor pressure. The radiative cooling effect induces a substantial temperature reduction at the M3 surface ($T_{\text{Amb}} > T_{\text{M3}}$). Given the exponential temperature dependence of saturated vapor pressure described by the Equation S7, this thermal contrast may create a localized saturation condition ($P_{\text{sat.}}(T_{\text{Amb}}) > P_{\text{sat.}}(T_{\text{M3}})$), resulting in an elevated effective RH near M3 compared to the ambient environment ($\Phi' > \Phi$).

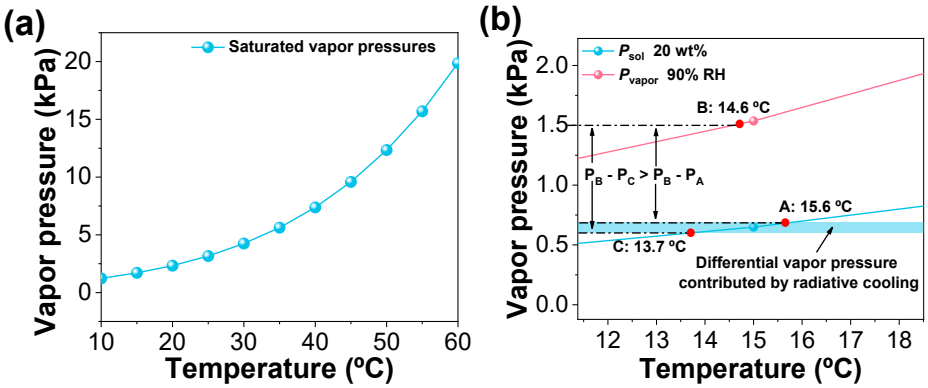

Figure S19. (a) The saturated vapor pressure of water at various temperatures under 1 standard atmosphere, and (b) illustration of the enhanced P_{vapor} difference generated by radiative cooling effect.

17. Water desorption characterization

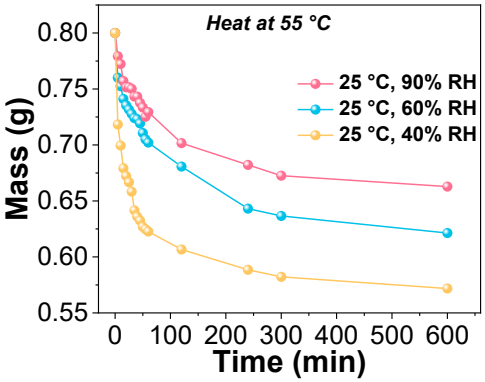

Figure S20. Weight changes of M3 during desorption under different RHs.

18. EDS images

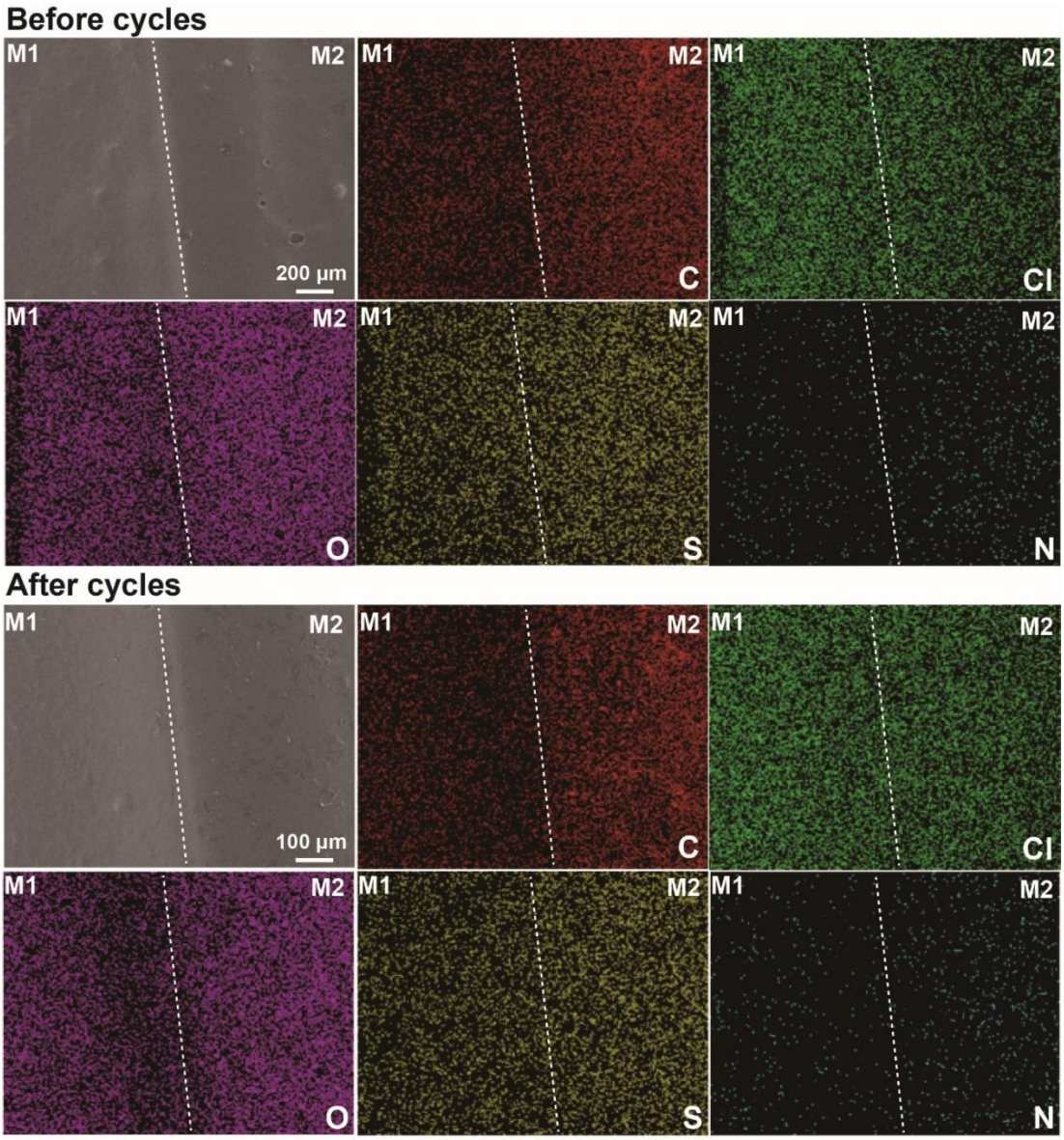

Figure S21. EDS images of M3 before and after sorption−desorption cycles.

19. IR images of solar cells

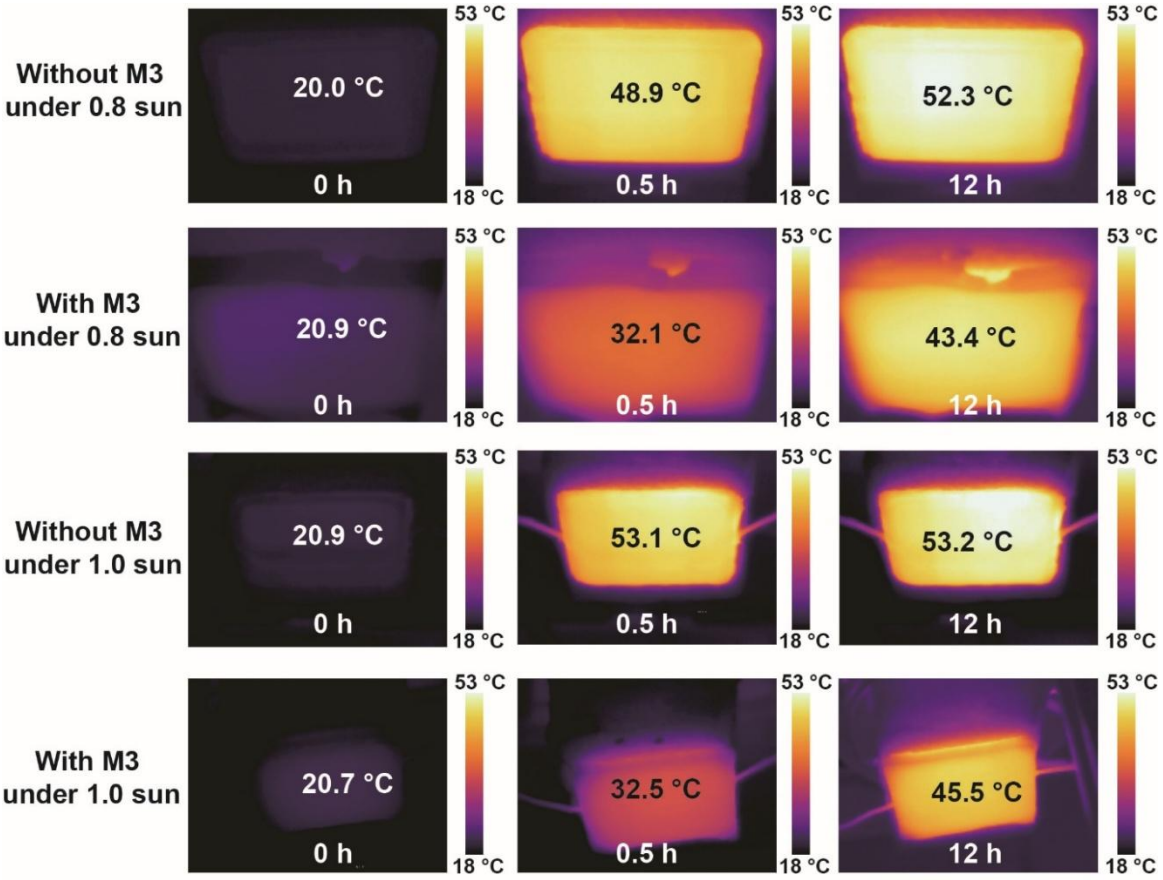

Figure S22. IR images of solar panels with and without M3 under 0.8 and 1.0 sun over time.

20. Photovoltaic parameters of solar cells without and with M3

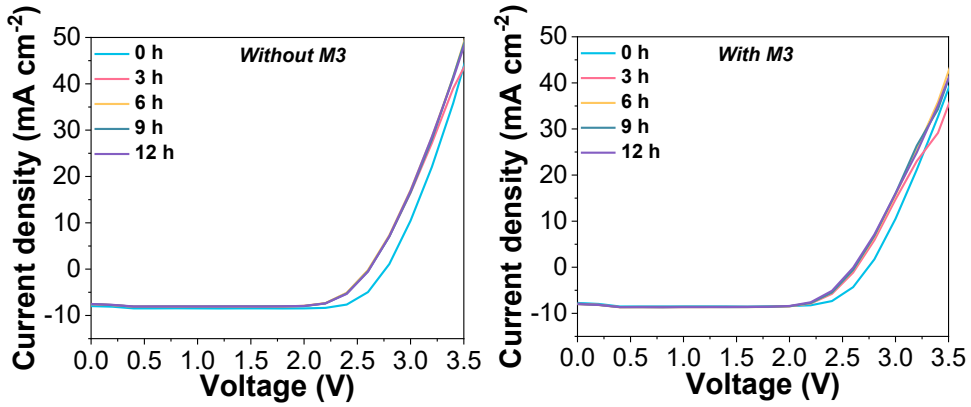

Figure S23. *J*–*V* curves of solar cells without and with M3 under 1 sun over 12 h.

Table S3. Photovoltaic parameters of a conventional solar cell under 1 sun.

Time (h)	V_{oc} (V)	J_{sc} (mA cm^{-2})	FF	PCE (%)
0	2.607	8.5	0.83	18.39
0.5	2.615	8.1	0.78	16.52
1	2.612	8.1	0.77	16.29
1.5	2.601	8.1	0.77	16.22
2	2.607	8.1	0.76	16.05
2.5	2.593	8.1	0.78	16.38
3	2.596	8.1	0.77	16.19
3.5	2.597	8.1	0.77	16.20
4	2.574	8.1	0.78	16.26
4.5	2.596	8.1	0.77	16.19
5	2.594	8.1	0.77	16.18
5.5	2.588	8.1	0.77	16.14
6	2.583	8.1	0.77	16.11
6.5	2.588	8.1	0.77	16.14
7	2.588	7.9	0.79	16.15
7.5	2.587	8.1	0.77	16.12
8	2.586	8.1	0.78	16.34
8.5	2.585	8.1	0.78	16.33
9	2.575	8.1	0.78	16.27
9.5	2.581	8.1	0.77	16.10
10	2.581	8.0	0.79	16.31
10.5	2.575	8.1	0.78	16.27
11	2.586	8.1	0.77	16.13
11.5	2.583	8.1	0.78	16.32
12	2.574	8.1	0.78	16.26

Table S4. Photovoltaic parameters of the M3-covered solar cell under 1 sun.

Time (h)	V_{oc} (V)	J_{sc} (mA cm^{-2})	FF	PCE (%)
0	2.629	8.7	0.80	18.30
0.5	2.608	8.6	0.81	18.17
1	2.605	8.4	0.82	17.94
1.5	2.603	8.5	0.81	17.92
2	2.606	8.6	0.78	17.48
2.5	2.597	8.6	0.78	17.42
3	2.609	8.6	0.77	17.28
3.5	2.599	8.6	0.77	17.21
4	2.603	8.6	0.77	17.24
4.5	2.606	8.7	0.76	17.23
5	2.603	8.7	0.77	17.44
5.5	2.596	8.7	0.77	17.39
6	2.600	8.7	0.76	17.19
6.5	2.606	8.7	0.76	17.23
7	2.608	8.7	0.75	17.02
7.5	2.611	8.7	0.75	17.04
8	2.601	8.7	0.75	16.97
8.5	2.604	8.7	0.75	16.99
9	2.609	8.6	0.76	17.05
9.5	2.606	8.6	0.75	16.81
10.5	2.509	8.7	0.77	16.81
11	2.413	8.6	0.81	16.81
12	2.407	8.6	0.81	16.77
48	2.377	8.7	0.80	16.55

21. P_{max} changes of solar cells

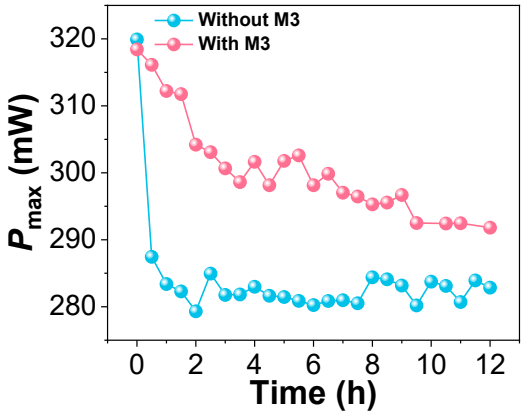

Figure S24. P_{max} variations of solar cells with and without M3 under 1 sun over time.

22. Summary of cooling performance of hygroscopic hydrogels

Table S5. Summary of cooling power and cooling capacities of hygroscopic hydrogels used for solar cells.

Time (h)	Cooling power (W m^{-2})	Cooling capacity (kW h m^{-2})	Ref.
6	151.99	0.91	[5]
3	294.90	0.88	[6]
2	529.00	1.06	[7]
3	298.00	0.89	[8]
1	108.89	0.11	[9]
6	133.84	0.80	[10]
3	121.50	0.36	[11]
2.5	315.00	0.79	[12]
3	288.20	0.86	[13]
1	463.79	0.46	
3	395.14	0.97	
6	323.82	1.21	This work
9	144.15	1.30	
12	112.24	1.35	

23. Summary of main parameters of different cooling methods

Table S6. Summary of cooling method, transmittance, emittance, water uptake, solar temperature reduction and solar efficiency enhancement of passive cooling materials used for solar cells reported so far.

Cooling method	Transparent, Transmittance (%)	Emittance (%)	Water uptake ($g\ g^{-1}$)	△T (°C)	Efficiency increase (%)	Ref.
Radiative cooling	Yes, ~90%	/	0	8.8	/	[14]
	Yes, 91%	98%	0	8.5	0.91, 8.7%	[15]
	Yes, 97%	98%	0	/	0.62, 3.2%	[16]
	Yes, 94%	96%	0	/	0.55, 3.1%	[17]
Evaporative cooling	Yes, /	0	/	17.0	1.00, 6.9%	[5]
	No	0	1.60	10.0	0.80, 6.8%	[6]
	No	0	1.75	26.0	/	[7]
	No	0	7.60	5.0	0.50, 5%	[8]
	Yes, /	0	/	8.0	0.35, 4.0%	[9]
	Yes, /	0	0.78	7.5	/	[10]
	No	0	1.20	5.8	/	[12]
	No	0	2.44	9.9	0.74, 5.9%	[13]
Hybrid cooling	Yes, 96%	95%	0	9.1	/, 4.8%	[18]
	Yes, 90%	98%	0.83	7.7	1.7, 10.4%	This work

24. Characterization of M3-covered solar cells under continuous irradiation

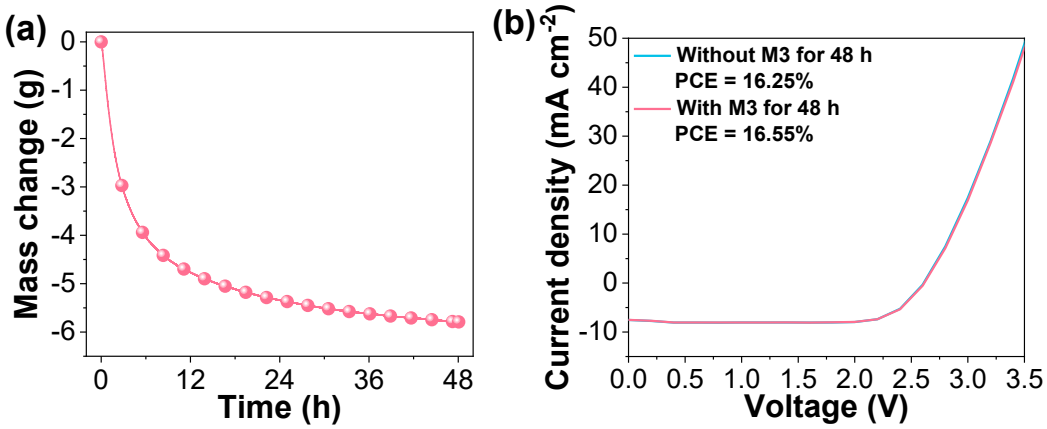

Figure S25. (a) Mass change of M3 under 1 sun over 48 h. (b) *J*–*V* curves of solar cells without and with M3 under 1 sun after 48 h.

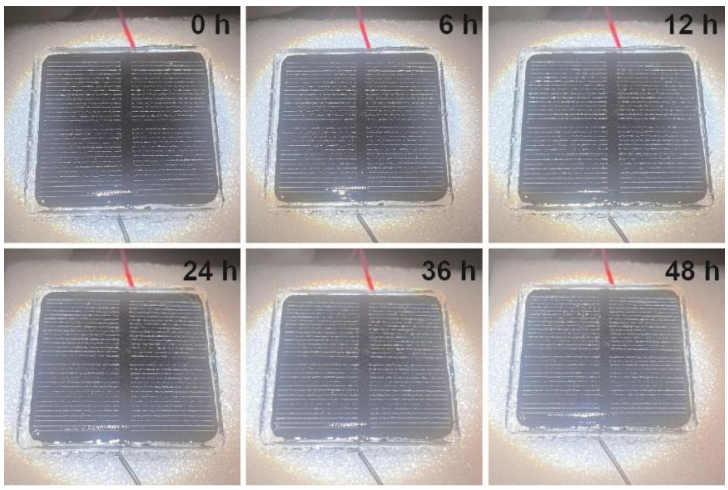

Figure S26. Image sequence of M3 under 1 sun over 48 h.

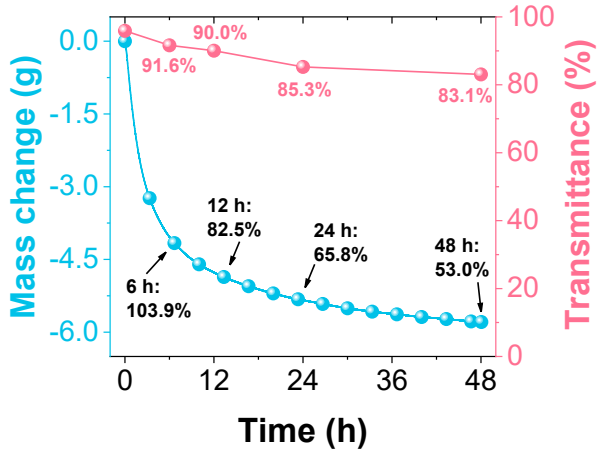

Figure S27. Changes of water weight, water contents and average transmittance of M3 over time under 1 sun.

25. Maximized PCE differences under real sky

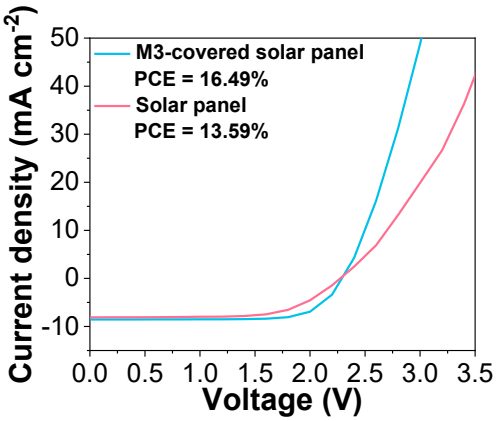

Figure S28. *J*–*V* curves of solar cells when maximized △PCE = 2.9% was achieved under real sky.

26. LiCl leakage characterization

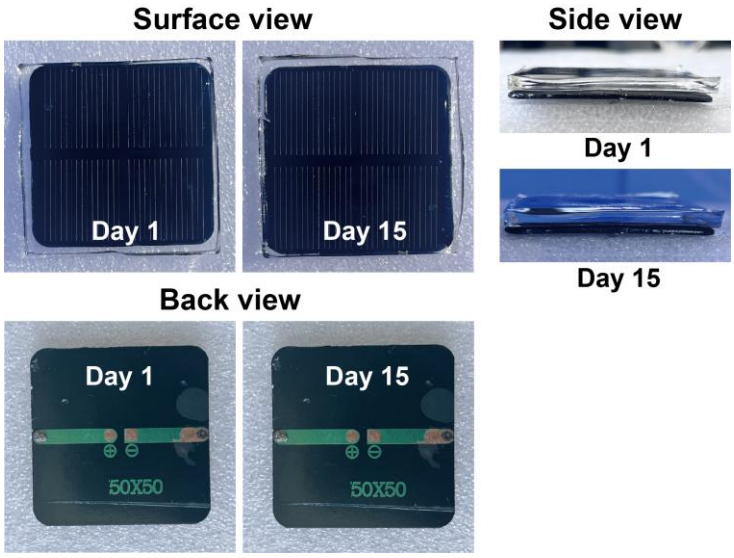

Figure S29. Sequential images of an M3-covered solar cell placed under outdoor conditions for 15 days.

27. Outdoor exposure characterization

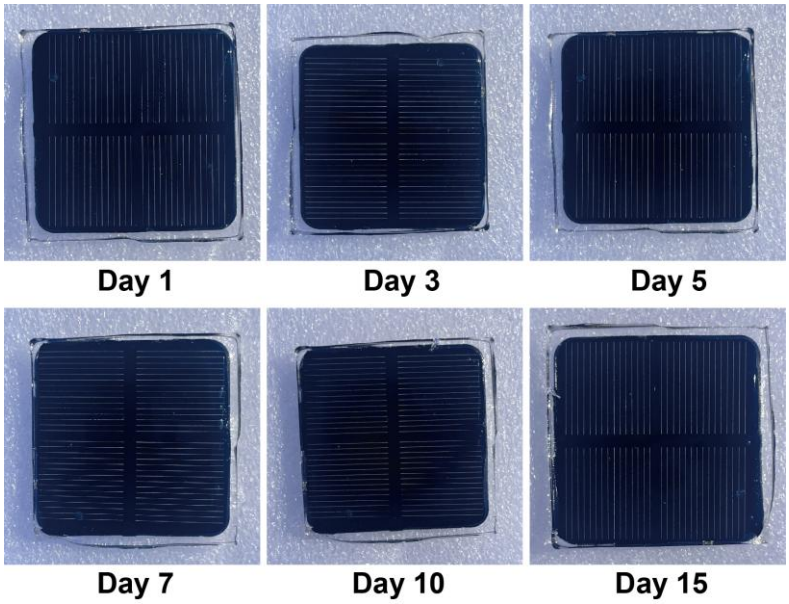

Figure S30. Image sequence of M3-covered *c*-Si solar cell during 15 days of outdoor exposure.

28. Cleanable surface property

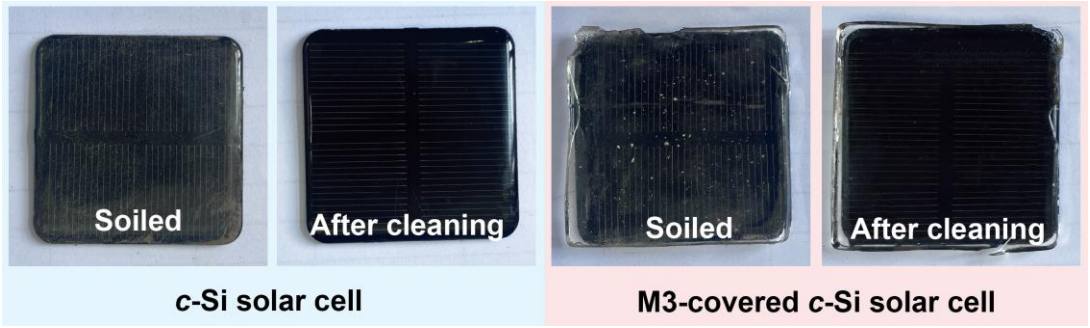

Figure S31. Digital photographs of conventional and M3-covered *c*-Si solar cells before and after manual cleaning.

29. Absorption coefficients of materials

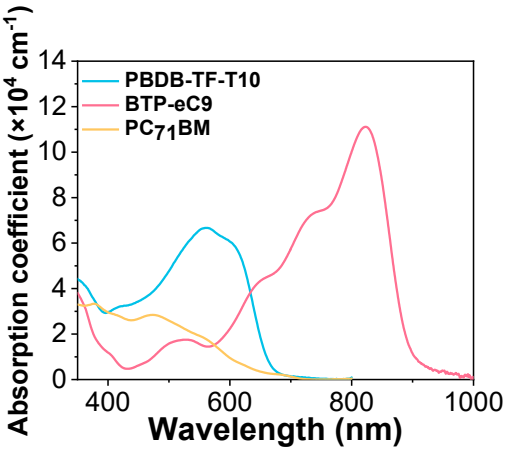

Figure S32. Absorption coefficients of PBDB-TF-T10, BTP-Ec9 and $PC_{71}BM$.

30. Photovoltaic parameters of flexible PSCs over illumination

Table S7. Summary of photovoltaic parameters of flexible PSCs before and after continuous illumination

	illumination duration	V_{oc} (V)	J_{sc} (mA cm^{-2})	FF	PCE (%)	Normalized PCE
Without M3	0 min	0.601	22.2	0.49	6.54	1.00
Without M3	20 min	0.577	22.8	0.47	6.18	0.94
With M3	0 min	0.631	21.5	0.49	6.65	1.00
With M3	20 min	0.615	21.2	0.50	6.52	0.98

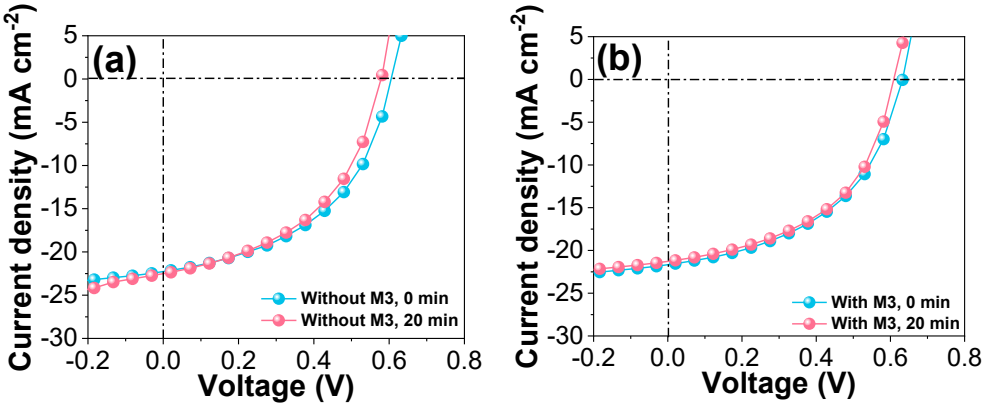

Figure S33. *J*–*V* curves of flexible PSCs (a) without and (b) with M3 before and after continuous illumination.

31. Photovoltaic parameters of flexible PSCs over bending

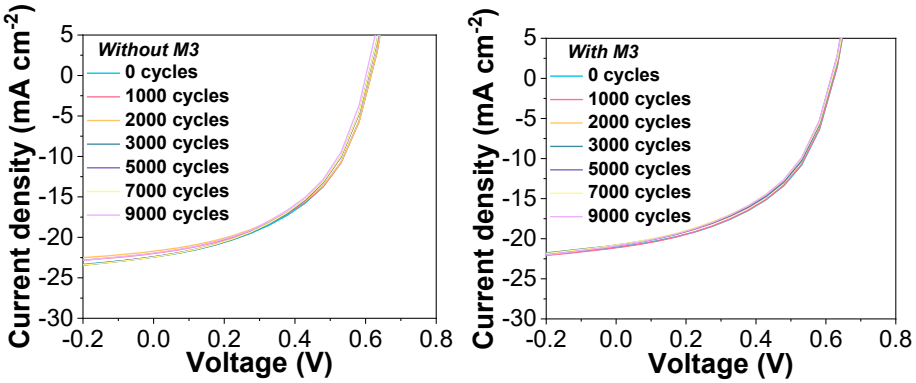

Figure S34. *J*–*V* curves of flexible PSCs without and with M3 in bending cycles.

Table S8. Summary of photovoltaic parameters of flexible PSCs in bending cycles

Number of bends	V_{oc} (V)	J_{sc} (mA cm^{-2})	FF	PCE (%)	Normalized PCE
0	0.615	22.5	0.49	6.77	1.00
1000	0.615	21.9	0.50	6.74	1.00
2000	0.615	21.7	0.50	6.67	0.99
3000	0.608	22.2	0.49	6.62	0.98
5000	0.609	22.5	0.48	6.57	0.97
7000	0.608	22.5	0.48	6.56	0.97
9000	0.601	21.5	0.50	6.46	0.95

Table S9. Summary of photovoltaic parameters of flexible PSCs with M3 in bending cycles

Number of bends	V_{oc} (V)	J_{sc} (mA cm^{-2})	FF	PCE (%)	Normalized PCE
0	0.623	20.9	0.50	6.52	1.00
1000	0.623	20.8	0.50	6.49	1.00
2000	0.619	20.5	0.50	6.36	0.98
3000	0.619	20.8	0.49	6.32	0.97
5000	0.615	20.7	0.49	6.24	0.96
7000	0.618	21.0	0.48	6.22	0.95
9000	0.615	21.0	0.48	6.21	0.95

32. Surface temperature changes over bending

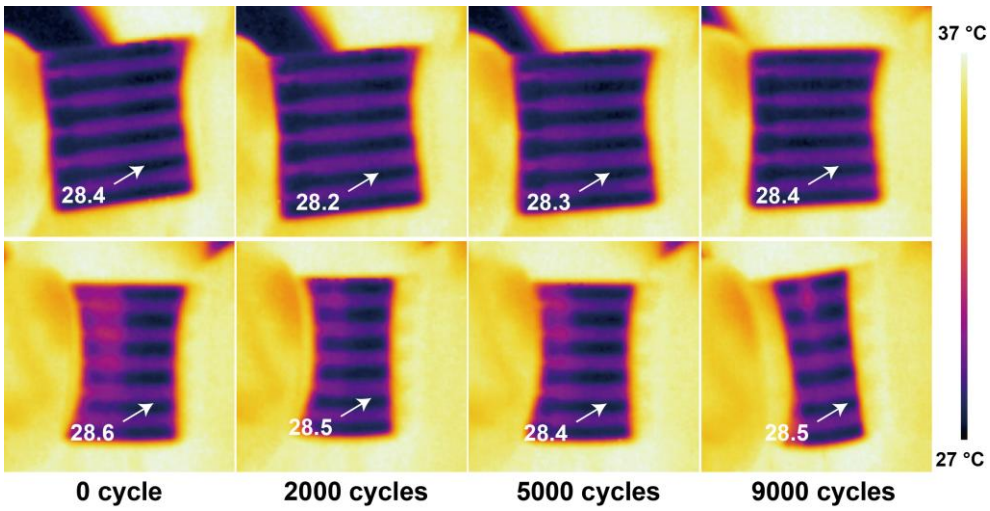

Figure S35. Surface temperature variations of flexible PSCs during bending cycles.

33. Reference

[1] Y. Xu, Q. Ji, L. Yin, N. Zhang, T. Liu, N. Li, X. He, G. Wen, W. Zhang, L. Yu, P. Murto, X. Xu, *ACS Appl. Mater. Interfaces* **2021**, 13, 23993.

[2] M. R. Conde, *Int. J. Therm. Sci.* **2004**, 43, 367.

[3] Y. Huang, Q. Li, Z. Chen, M. Chen, *J. Colloid Interface Sci.* **2024**, 655, 527.

[4] R. Peeters, H. Vanderschaeghe, J. Rongé, J. A. Martens, *Environ. Sci.: Water Res. Technol.* **2020**, 6, 2016.

[5] S. Pu, J. Fu, Y. Liao, L. Ge, Y. Zhou, S. Zhang, S. Zhao, X. Liu, X. Hu, K. Liu, J. Chen, *Adv. Mater.* **2020**, 32, 1907307.

[6] R. Li, Y. Shi, M. Wu, S. Hong, P. Wang, *Nat. Sustain.* **2020**, 3, 636.

[7] H. Li, J. Ma, W. Yan, J. Lan, W. Hong, *Renew. Energy* **2024**, 235, 121277.

[8] J. He, N. Li, S. Wang, S. Li, C. Wang, L. Yu, P. Murto, X. Xu, *J. Mater. Chem. A* **2022**, 10, 8556.

[9] Z. Zhou, Y. Zhang, W. Liu, C. Gui, L. Huang, H. Huang, K. Fan, Y. Huang, Y. Gong, A. Chen, P. Liu, H. Jiang, *Desalination* **2024**, 583, 117685.

[10] Z. Li, T. Ma, F. Ji, H. Shan, Y. Dai, R. Wang, *ACS Energy Lett.* **2023**, 8, 1921.

[11] J. Li, C. Xu, L. Chen, X. Zhang, M. Zhu, Y. Cheng, *Adv.Funct. Mater.* **2025**, 35, 2423063.

[12] G. Wang, Y. Li, H. Qiu, H. Yan, Y. Zhou, *Droplet* **2023**, 2, e32.

[13] Y. Liu, Z. Liu, Z. Wang, W. Sun, F. Kong, *Appl. Therm. Eng.* **2024**, 240, 122185.

[14] S.-Y. Heo, D. H. Kim, Y. M. Song, G. J. Lee, *Adv. Energy Mater.* **2022**, 12, 2103258.

[15] K. W. Lee, W. Lim, M. S. Jeon, H. Jang, J. Hwang, C. H. Lee, D. R. Kim, *Adv. Funct. Mater.* **2022**, 32, 2105882.

[16] S. Lin, L. Ai, J. Zhang, T. Bu, H. Li, F. Huang, J. Zhang, Y. Lu, W. Song, *Sol. Energy Mater. Sol. Cells* **2019**, 203, 110135.

[17] Y. Lu, Z. Chen, L. Ai, X. Zhang, J. Zhang, J. Li, W. Wang, R. Tan, N. Dai, W. Song, *Sol. RRL* **2017**, 1, 1700084.

[18] J. Shang, J. Zhang, Y. Zhang, X. Zhang, Q. An, *Nano Lett.* **2024**, 24, 7055.